Research Square

Preprints are preliminary reports that have not undergone peer review.
They should not be considered conclusive, used to inform clinical practice,
or referenced by the media as validated information.

Effect of Heat Treatment on Microstructure and Mechanical Properties of Additively Manufactured Inconel 718 alloy Optimized Using a Modified Taguchi Method

Prasanth Kumar Reddy Kurre
kprasanthkumarreddy@gmail.com

SRM University, Andhra Pradesh

Sheela Singh
SRM University, Andhra Pradesh

Kartikey Sharma
Indian Institute of Technology Bombay

Nageswara Rao B
Koneru Lakshmaiah Education Foundation

Narayana Murty S.V.S.
ISRO Propulsion Complex

Ravi Ranjan Kumar
ISRO Propulsion Complex

Research Article

Keywords: Selective Laser Melting (SLM), Hot isostatic pressing (HIP), Modified Taguchi Method, Yield strength (YS), Ultimate tensile strength (UTS)

Posted Date: March 2nd, 2026

DOI: https://doi.org/10.21203/rs.3.rs-8728436/v1

License: This work is licensed under a Creative Commons Attribution 4.0 International License. Read Full License

Additional Declarations: No competing interests reported.

Abstract

This study optimizes Selective Laser Melting (SLM) parameters for Inconel 718 (IN718) using a modified Taguchi approach and investigates the effects of heat treatments and build orientations (XY and XZ) on the mechanical properties. Experiments were performed with constant hatch distance (0.11 mm) and powder bed thickness (0.04 mm), while laser power (300–400 W) and scanning speed (520–1400 mm/s) were varied. The modified Taguchi's method was employed for selecting optimal parameters, a laser power of 360 W and scanning speed of 960 mm/s yielded the best mechanical performance. In the as-printed condition, IN718 exhibited a yield strength (YS) of 774 ± 96 MPa, ultimate tensile strength (UTS) of 1141 ± 81 MPa, elongation (%El) of 31 ± 10%, and hardness of ~ 355 HV. After solution treatment and aging (STA), the strength increased significantly (YS = 1286 ± 129 MPa; UTS = 1516 ± 130 MPa, and hardness = 535 HV), while elongation decreased to 22 ± 4% due to γ'/γ" precipitation hardening. Hot isostatic pressing followed by STA resulted in slightly reduced strength (YS = 1163 ± 171 MPa; UTS = 1444 ± 64 MPa; %El = 21 ± 3%), attributed to grain coarsening during HIPing. Build orientation influenced anisotropy: XY builds exhibited higher strength and hardness (~ 535 Hv), XZ builds showed higher ductility up to 20–25%. Microstructural analysis revealed porosity and columnar grains in as printed samples, strengthened columnar structures after STA, and equiaxed recrystallized grains after HIP + STA. Overall, the combination of optimized SLM parameters and suitable heat treatments enables the fabrication of dense, defect-free IN718 components with superior mechanical properties for aerospace applications.

1. Introduction

Additive manufacturing (AM) technologies, particularly Selective Laser Melting (SLM), have gained significant attention for producing complex, high-performance components in aerospace and space applications[1, 2]. Among the materials suitable for such applications, Inconel 718 (IN718), a nickel-based superalloy, possesses high-temperature strength, corrosion resistance, and fatigue performance [3–6].Achieving optimal mechanical properties in SLM-fabricated IN718 requires careful control over process parameters and post-processing treatments.

The SLM process involves numerous parameters, such as laser power, scanning speed, hatch distance, and layer thickness, all of which affect the microstructure and final properties of the printed part. Additionally, build orientation and post-processing heat treatments like solution treatment and aging (STA) and hot isostatic pressing (HIP) play a critical role in enhancing the mechanical performance and reducing internal defects such as porosity. Understanding the interaction between these process parameters is essential for enhancing material properties for aerospace applications.

Solution treatment and age hardening (STA) has a crucial role in the mechanical properties of the sample, from the literature; Sharma et al.[7] studied the effect of heat treatment variations, including homogenization, solution treatment, and double aging followed by furnace cooling and then air cooling of double aging. It was observed that after double aging offers superior mechanical properties. Wang et al.[8] examined the effects of homogenization, solution treatment, and double ageing. After double aging heat treatment, very little precipitation of γ'/γ" phases was observed. After solution treatment and aging treatment, the amount of precipitation observed at grain boundaries was seen to increase. Prominent amount of precipitation of γ'/γ" was observed while laves phase was entirely solid-dissolved after HSA heat treatment. The amount of precipitation observed of strengthening phase can be controlled by controlling heat treatment.

The SLM process creates distinctive microstructures, whereas the hot isostatic pressing (HIP) process alters the microstructure thus it influences mechanical properties and creep behaviour [9]. Combining SLM with HIP can enhance creep resistance and material densification but might also pose challenges related to high-temperature ductility [10–12]. The main differences between SLM and HIP for IN718 lie in their microstructure, mechanical properties, and the distribution of second phase particles[13]. SLM-produced materials have a microstructure free of oxide layer, oxide particles, and other prior particle boundaries (PPB), while HIP-treated materials exhibit a coarse recrystallized gamma matrix phase with continuous precipitates along the PPB [14, 15]. Furthermore, SLM materials show lower strength and ductility compared to wrought materials due to environmental sensitivity and brittle intergranular fracture [16]. In contrast, HIP treatment significantly refines the microstructure of superalloys by eliminating defects and promoting a more homogeneous and finer distribution of

strengthening gamma-prime (γ') precipitates, which drastically improves mechanical properties like tensile strength, ductility, and density, creating a balanced, robust material for high-temperature applications. This uniform precipitate structure hinders dislocation movement, enhancing overall performance [10–12].

SLM materials, after undergoing STA, demonstrated mechanical properties comparable to conventional wrought specimens at room temperature and 650 ºC [7]. However, a reduction in ductility was noted for HIP materials at 650 ºC [12]. The HIP process was effective in enhancing creep behaviour at 650 ºC, with the creep rupture life extending to nearly 800 hours due to the elimination of pores that prevent microcrack nucleation [11]. This process also eliminated casting porosity defects, improved alloy homogenization, and altered the size and quantity of the γ" phase in IN718C [17].

The challenges in achieving high-density IN718 parts using SLM and HIP processes are, the SLM fabricated materials can be results in uneven grain sizes since heavy distortion or high-density dislocation, which can negatively impact mechanical properties. The standard heat treatment recommended for cast and wrought materials is ineffective for SLM-processed specimens, highlighting the need for customized post-processing methods. The HIP process effectively improves creep behaviour by preventing microcrack nucleation and enhancing resistance to creep rupture. Despite its benefits, HIP as a post-processing step adds significant cost and time, thus affecting the productivity of additive manufacturing processes. Hence, understanding the combined influence of optimized SLM parameters and post-processing heat treatments is essential to tailor IN718 properties for aerospace-grade performance.

This study aims to optimize the SLM process for IN718 using a modified Taguchi method and assess the influence of different heat treatments on the alloy's mechanical behavior. Key mechanical properties including yield strength (YS), ultimate tensile strength (UTS), and elongation (%El) are evaluated under different conditions: as-printed (AP), STA, and HIP followed by STA. Statistical consistency of experimental data is validated using Chauvenet’s criterion. Microstructural analysis and mechanical anisotropy with respect to build orientation are also investigated [18]. The outcomes provide a validated framework for producing dense, defect-free IN718 components for high-performance aerospace applications.

2. Materials and Methods

The chemical composition of the IN718 consistent with the generally accepted composition ranges in AMS 5662 standard in this study is: Ni (53.3%), Cr (19.15%), Nb (4.99%), Mo (3.19%), Ti (1.1%), Al (0.48%), and Fe (Balance). For the experimental setup, IN718 cubes were fabricated using selective laser melting (SLM) with 300–400 W laser powers, 520–1400 mm/s scanning speeds, 0.11 mm hatch distance, 0.04 mm powder bed layer thickness, and each successive layer was rotated by 67°. Density measurements were conducted using Archimedes' method according to ASTM B962-17. Microstructural analysis involved an optical microscope to identify defects like porosity and lack of fusion. Tensile test specimens were machined from the cubes in two orientations (XY and XZ planes) and tested at room temperature (ASTM E8) using a universal testing machine. Heat treatments like Solution Treatment and Aging (STA) and Hot Isostatic Pressing plus STA (HIP + STA) are essential for SLM IN718 to transform the brittle, as-built microstructure into a high-strength, homogenized state suitable for aerospace and industrial use. A modified Taguchi L9 orthogonal array was employed for experimental design and optimization of process parameters (laser power, scanning speed, and post-heat treatment), focusing on maximizing yield strength (YS). The analysis incorporated Chauvenet's criterion for statistical validation and to provide estimated ranges for mechanical properties.

2.1 Heat Treatment Process

Printed cube was sectioned using an electro-discharge machine (EDM) into three slices measuring 40 × 30 × 8 mm. Each slice was then subjected to heat treatment cycles (see Table-1): As-printed (AP), solution treatment and aging (STA), and hot isostatic pressing followed by solution treatment and aging (HIP + STA) in accordance with ASTM 3055 [19]. Subsequently, each heat-treated slice was further sectioned by EDM to obtain three miniature tensile specimens with a gauge length of 6 mm (4D), prepared in two build directions (XY and XZ) can be seen in Fig. 1. This process resulted in three tensile specimens for both build directions.

Table 1. Heat Treatment Designation for SLM samples [7,19]

Heat Treatment	Heat Treatment Details	Graph
As Printed (AP)	As Printed – No heat treatment	NIL
Solution treatment by age hardening (STA)	Solution treatment at 980°C for 1 hr followed by water quenching. Followed by Double aging at 720° C for 8 hr followed by Furnace Cooling at 55° C/hr to 620° C. Holding at 620° C for 8 hr followed by Air Cooling	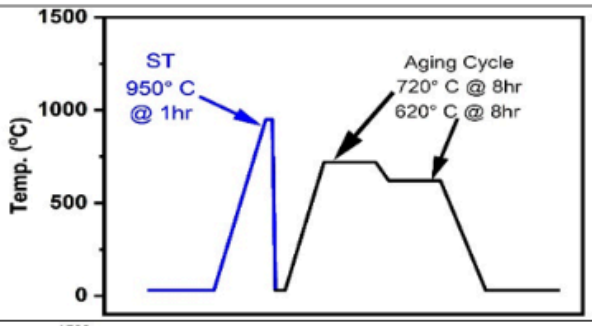
Hot Iso-static Pressing (HIP) + STA	Hot iso-static pressing at 1120° C for 3 hr at 160 bar of pressure followed by Furnace cooling followed by STA	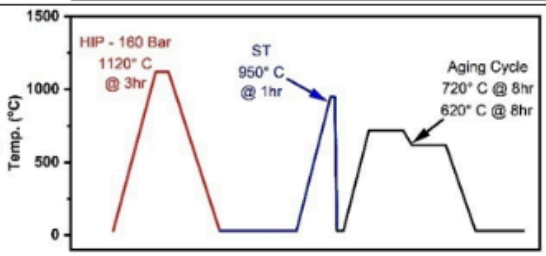

Initially the samples were fabricated in the as-printed (AP) condition with dimensions of 25 × 40 × 30 mm. As in Table-1, the specimens were then subjected to different heat treatment sequences (AP, STA, and HIP + STA). For the HIP + STA route, hot isostatic pressing was performed at 1120°C under a pressure of 160 bar for 3 hours. The solution treatment (ST) was carried out at 980°C for 2 hours. Subsequently, aging was conducted using a two-step aging cycle consisting of 720°C for 8 hours followed by 620°C for 8 hours. For comparison, one set of samples underwent only STA, while another set followed the complete HIP + STA sequence. After heat treatment, specimens were sectioned and machined into tensile samples in both XY and XZ orientations. The extracted specimens had specific geometrical features, including a gauge length of 25 mm, section widths of 7 mm, a fillet radius of R1.5, and thicknesses of 0.9 mm.

2.2 Modified Taguchi's Method

Inconel 718 was printed in the form of cuboids using an EOS M 290 machine. For the three parameters (laser power, scanning speed, and heat treatment process) with three levels, Taguchi's L_9 orthogonal array (OA), is selected in the design of experiments presuming no interaction between the parameters. According to the Taguchi's L_9 OA, for levels to each SLM parameter, the number of input parameters () can be found from [1, 2]:

$$N_{Tag} = 1 + n_p\,(n_l - 1) \Rightarrow\ n_p = \frac{(N_{Tag} - 1)}{(n_l - 1)} = \frac{(9-1)}{(3-1)} = \frac{8}{2} = 4$$

For 9 tests, 4 input parameters can be accommodated. In this case, only 3 SLM process parameters (i.e. LP, SS, and HT) were set and hence, a fictitious parameter (f) is introduced in Table 2 to assess the error in estimates as in [1, 2]. Meander scanning strategy was employed for printing, as this strategy has been reported to yield better mechanical properties and relative density (> 99%) [20]. Table 3 prepared in accordance with Taguchi's L_9 OA.

Table 2
SLM process parameters used in the present study

Process Parameters	Level – 1	Level – 2	Level – 3
Laser power (LP)	300	360	400
Scanning Speed (SS)	520	960	1400
Heat treatment (HT)	AP	STA	HIP + STA
Fictitious (f)	f1	f2	f3

Table 3
IN718 samples prepared as per Taguchi's L_9 Orthogonal array

Test SNo	LP	SS	HT	f
1	300	520	AP	f1
2	300	960	STA	f2
3	300	1400	HIP + STA	f3
4	360	520	STA	f3
5	360	960	HIP + STA	f1
6	360	1400	AP	f2
7	400	520	HIP + STA	f2
8	400	960	AP	f3
9	400	1400	STA	f1

In the design of experiments, selection of optimal SLM process parameters is the main goal to fabricate IN718 components with minimal defects and enhanced mechanical properties after heat treatment. The SLM process parameters within this investigation were systematically varied: laser power (LP) ranged from 300 W to 400 W, and scanning speed (SS) was adjusted between 520 mm/s to 1400 mm/s. The levels of heat treatment (HT) are AP, STA, and HIP + STA. The key metrics used to evaluate the fabricated parts' performance included their percentage elongation at break (%el), the 0.2% yield strength (YS), and the ultimate tensile strength (UTS).

To efficiently explore the parameter space, Taguchi's L_9 OA was employed, an experimental design well suited for studies involving up to four process parameters, each assigned at three distinct levels. This study utilizes a modified version of the Taguchi method as evidenced in works by [1, 2, 21–23]. This adaptation was essential for identifying the optimal process parameters and for formulating empirical relationships that link the chosen input process variables to the observed output responses.

A notable distinction of this modified Taguchi method, which incorporates Chauvenet's criterion, is its capacity to provide a range of estimated values for the output responses, rather than merely providing the optimal solution compared to the average of repeated tests – a usual practice among other researchers. This provision of an estimated range is particularly valuable when conducting repeated tests across the entire spectrum of input process variables. Indeed, Chauvenet's criterion served as tool for the statistical validation of repeated test data [24, 25], whose application facilitated the determination of statistically permissible limits, thereby verifying the acceptable scatter in the data and ensuring the statistical consistency of the repeated measurements. This criterion relies on the assumption that the data adheres to a normal distribution. If the data significantly deviate from normality, then non-parametric statistical tests, such as Grubbs's test or Dixon's Q-test, would be more appropriate.

For instances involving three 3 repeated tests yielding three output responses (η_1, η_2, η_3), the calculations for Chauvenet's criterion are as follows.

- The mean value ($\bar{\eta}$) is calculated as : $\bar{\eta} = \frac{1}{3}(\eta_1 + \eta_2 + \eta_3)$
- The standard deviation (η_σ), is determined by:

$$\eta_\sigma = \sqrt{\frac{1}{2}\left\{(\eta_1 - \bar{\eta})^2 + (\eta_2 - \bar{\eta})^2 + (\eta_3 - \bar{\eta})^2\right\}}$$

- The calculated allowable lower limit, $\eta_{LL} = \bar{\eta} - 1.38 \times \eta_\sigma$
- The calculated allowable upper limit, $\eta_{UL} = \bar{\eta} + 1.38 \times \eta_\sigma$.

As in literature [2, 23, 25, 26], Chauvenet's criterion is applied to the output responses of the repeated tests and determined the statistically allowable limits (Lower limit (LL) and Upper limit (UL)) to verify the acceptance of scatter in the repeated test data. Chauvenet's criterion delivering acceptable range of values for repeated test data through the use of average (AVE) and standard deviation (SD), Table 4 represents the lower bound (LB) and upper bound (UB). Application of the Chauvenet's criterion on the repeated test values of each test run will be helpful to trace and discard the statistically unacceptable values (if any).

Table 4
Acceptable limits (LL and UL) of the mechanical properties using Chauvenet's criterion for IN718 specimens (XY & XZ – Build direction)

XY						**XZ**				
SNo.	**Test Data**			**Chauvenet's criterion**		**Test Data**			**Chauvenet's criterion**	
	Elongation (%)			**LL**	**UL**	**Elongation (%)**			**LB**	**UB**
1	32.2	32.5	32.5	32.1	32.7	38	39	37	36.1	39.4
2	19.6	19.3		19.2	19.6	20	19	18	17.5	20.4
3	22.2	22.5	21.2	21.0	22.9	23	20	19	17.7	23.1
4	17.5	20.8	15.3	14.1	21.7	18	22	19	17.1	22.1
5	20.8	20.5		20.4	20.9	26	30	-	25.3	30.7
6	30.2	39.2	35.8	28.8	41.3	36	28	33	26.8	37.7
7	22.2	26.0		21.0	27.2	22	25	-	21.2	25.5
8	34.5	32.7	24.2	22.8	38.1	34	42	41	32.6	45.4
9	20.3	20.0	15.8	15.3	22.2	19	13	18	12.3	20.5
SNo.	**YS (MPa)**			**LL**	**UL**	**YS (MPa)**			**LL**	**UL**
1	803.4	720.6	650.2	619.1	830.5	646	654	491	469.8	724.1
2	1313.2	1329.2		1308.1	1334.2	1274	1277	1192	1181.2	1314.5
3	1227.8	1215.3	928.9	890.7	1357.3	1180	1254	1106	1077.6	1282.2
4	1153.0	1253.1	1398.2	1098.1	1438.2	1204	1201	1116	1104.7	1242.5
5	1208.4	1155.8		1139.3	1224.9	1237	1128	-	1094.1	1271.4
6	743.0	803.7	753.3	721.9	811.4	742	712	572	549.8	800.4
7	1215.1	1150.2		1129.9	1235.4	1346	1255	1245	1205.9	1358.3
8	794.3	820.7	533.7	497.3	935.2	620	865	667	537.6	897.3
9	1253.2	1326.5	1198.7	1171.1	1347.9	1263	1240	1445	1161.3	1471.3
SNo.	**UTS (MPa)**			**LL**	**UL**	**UTS (MPa)**			**LL**	**UL**
1	1122.1	1083.1	1057.5	1042.7	1132.4	1022	993	939	926.8	1042.8
2	1566.6	1485.8		1460.5	1591.9	1502	1471	1443	1437.7	1505.6
3	1461.2	1420.1	1375.8	1360.0	1478.1	1436	1426	1396	1390.1	1448.4
4	1434.0	1409.6	1473.6	1394.6	1483.6	1394	1373	1390	1370.2	1401.1
5	1447.3	1446.6		1446.4	1447.5	1475	1419	-	1401.6	1493.1
6	1202.6	1191.5	1049.5	1030.0	1265.7	1145	1116	996	976.4	1194.6
7	1481.3	1468.5		1464.6	1485.3	1515	1451	-	1431.3	1534.7
8	1153.0	1156.1	1063.2	1051.3	1196.9	1008	1090	983	949.2	1104.5
9	1524.5	1555.8	1568.9	1518.2	1581.3	1452	1409	1495	1392.6	1511.4

An ANOVA was performed on the LL and UL values of the output responses such as elongation (%), YS, and UTS in Table 4. Using the ANOVA results and applying the additive law, the LL and UL of output responses were estimated for the specified levels of the SLM process parameters (LP, SS, and HT). The corrections to these estimates are obtained as follows. The minimum deviation of the LL output responses corresponding to the mean values of fictitious parameter (f) from their grand mean values provide the corrections to obtain lower bound estimates, while the maximum deviation of the UL output responses corresponding to the mean values of the fictitious parameter (f) from their grand mean values to obtain upper bound estimates. Transforming the three levels of the SLM process parameters to -1, 0 and 1, it is possible to represent mean values of output responses in ANOVA Table in a quadratic polynomial form and use them in the additive law to obtain empirical relationships for LL and UL output responses in terms of input variables (LP, SS, HT).

Coefficients from the developed empirical relation (Eq. 1) by varying LP from 300 to 400 W: SS from 520 to 1400 mm/s at constant HS of 0.11 mm and PBT of 0.04 mm can be seen Table 5. Let ψ be the general function for output response, which can be expressed in terms of input variables as in Eq. 1.

$$\psi = \psi_0 + \psi_1\xi_1 + \psi_2\xi_1^2 + \psi_3\xi_2 + \psi_4\xi_2^2 + \psi_5\xi_3 + \psi_6\xi_3^2$$

1

Here, $\xi_1 = \frac{(LP-360)(LP-100)}{12000}$, and $\xi_2 = \frac{1}{440}(SS - 960)$. In case of heat treatment (HT) process, $\xi_3 = -1$ for AP; $\xi_3 = 0$ for STA; and $\xi_3 = 1$ for HIP + STA conditions.

Table 5
Coefficients in the developed Empirical relationship (Equation – 1) for the output responses.

XY build direction								
	$\varvec{\psi}$	$\varvec{\psi_0}$	$\varvec{\psi_1}$	$\varvec{\psi_2}$	$\varvec{\psi_3}$	$\varvec{\psi_4}$	$\varvec{\psi_5}$	$\varvec{\psi_6}$
LB	**%El**	12.4880	-2.206	0.815	-0.355	1.223	-3.564	8.175
	YS	1130.627	-3.274	-50.387	-10.539	-43.187	220.284	-359.349
	UTS	1413.371	28.474	25.904	1.076	-17.739	191.159	-225.256
UB	**%El**	21.8282	2.586	0.752	0.262	0.146	-6.834	9.335
	YS	1434.916	-0.598	15.266	2.099	5.381	206.745	-307.672
	UTS	1528.575	10.183	12.048	37.290	-7.697	135.976	-217.946
XZ build direction								
	$\varvec{\psi}$	$\varvec{\psi_0}$	$\varvec{\psi_1}$	$\varvec{\psi_2}$	$\varvec{\psi_3}$	$\varvec{\psi_4}$	$\varvec{\psi_5}$	$\varvec{\psi_6}$
LB	**%El**	16.814	-0.881	-0.165	-2.941	-3.293	-5.219	10.968
	YS	1115.558	29.370	22.667	1.375	-9.453	303.407	-326.598
	UTS	1390.260	3.073	5.225	5.134	-14.930	228.450	-220.934
UB	**%El**	25.299	1.443	-1.100	-0.948	-4.176	-7.207	12.618
	YS	1312.373	67.697	69.823	38.175	-14.614	248.342	-287.168
	UTS	1590.023	25.634	-5.011	29.295	-12.233	189.059	-169.678

For the combination of three levels of three SLM process parameters, 27 (= 3^3) sets were created: , in which subscripts to parameters (LP, SS, HT) are the levels. They represent the full factorial design of experiments and allotted the sequence

numbers from 1 to 27. The set of input parameters to the sequence numbers 1, 11, 21, 13, 23, 6, 25, 8, and 18 represent the test sequence numbers 1 to 9 in Taguchi's L_9 OA. The comparison between the measured mechanical properties and the estimated upper and lower limits obtained for both XY and XZ build directions of the full factorial (all 27 test parameters) experiments can be seen in the Fig. 2 and Fig. 3. In the XY direction (Figs. 2a–2c), %elongation, yield strength (YS), and ultimate tensile strength (UTS) generally fall within the predicted bounds, with a noticeable transition in properties around the mid-sequence experiments, indicating a strong influence of process parameter combinations. A similar trend is observed in the XZ direction (Figs. 3a–3c), where strength values (YS and UTS) show a significant increase after certain parameter sets, while elongation correspondingly decreases, highlighting the strength–ductility trade-off. Overall, the figures demonstrate good agreement between experimental results and estimated ranges, validating the robustness of the full factorial design approach in predicting mechanical performance across different build orientations.

3. Results and Discussion

To study the effect of laser power, scanning speed and heat treatment on the defects and microstructures the optical microscope was used. Previous studies [1, 2, 21]have shown how process parameters influence the density of SLM-fabricated IN718.

The influence of build direction and post-processing treatments on the mechanical properties is summarized in Table 6 and illustrated in Fig. 4. In the as-printed (AP) condition, the samples exhibited comparatively lower yield strength (684–774 MPa) and ultimate tensile strength (1069–1141 MPa), but higher elongation, particularly in the XZ build direction (39 ± 6%) compared to XY (31 ± 10%). This behavior can be attributed to the presence of residual porosity, lack-of-fusion defects, and anisotropic columnar grain growth along the build direction, which collectively limit load-bearing capability but promote ductility.

Upon applying solution treatment and aging (STA), a significant improvement in strength was observed in both build directions, with yield strength increasing to 1250–1286 MPa and UTS reaching 1488–1516 MPa. This strengthening effect is primarily governed by precipitation hardening, where γ' and γ" phases precipitate during aging and impede dislocation motion. However, elongation was reduced to 21–23%, reflecting the typical strength–ductility trade-off associated with fine precipitate formation.

The HIP + STA treatment produced an intermediate response, where strength values (YS: 1163–1183 MPa; UTS: 1444–1477 MPa) remained high but were slightly lower than STA, while elongation improved modestly (21–27%). This trend is attributed to the elimination of internal porosity and grain coarsening during HIPing.

From an application standpoint, these findings are particularly relevant to aerospace components manufactured via LPBF, where both high strength and adequate ductility are critical to sustain cyclic loading and prevent premature failure. While STA yields maximum strengthening, the reduced ductility may limit its suitability in service environments that demand damage tolerance. In contrast, HIP + STA provides a more favourable balance between strength and elongation, making it a promising post-processing route for critical load-bearing parts such as turbine blades, combustor components, and structural brackets in aerospace engines. The graphical comparison in Fig. 4 reinforces these trends, demonstrating that HIP + STA-treated samples offer the most application-relevant combination of mechanical properties.

Table 6
Results of optimal process parameter Laser Power is 360 W and Scanning Speed is 960 mm/s

XY – Build Direction			
Heat Treatment	Elongation (%)	Yield Strength (MPa)	UTS (MPa)
HIP + STA	21 ± 3	1163 ± 171	1444 ± 64
STA	21 ± 4	1286 ± 129	1516 ± 130
AP	31 ± 10	774 ± 96	1141 ± 81
XZ – Build Direction			
Heat Treatment	Elongation (%)	Yield Strength (MPa)	UTS (MPa)
HIP + STA	27 ± 4	1183 ± 91	1477 ± 79
STA	23 ± 3	1250 ± 99	1488 ± 33
AP	39 ± 6	684 ± 164	1069 ± 88

3.1 Effects of Heat Treatment on the Microstructural

Metallographic specimens were prepared based on the standard procedures of grinding-polishing-etching. Optical microscopy (OM) was used to get microstructures. Figure 4 clearly shows the increase in strength after STA condition as compared to AP condition. However, a decline in strength was observed after HIP + STA treatment, this due to the fact that the high temperature experienced during HIP process leads to grain coarsening [7], which leads to reduction in strength according to Hall-Petch relation.

In terms of heat treatment, it is well-known that the microstructure and mechanical properties of materials can be significantly altered by different heat treatment processes. Heat treatment involves heating the material to a specific temperature and then cooling it down at a specific rate to achieve certain desired properties. In the case of IN718, heat treatment is often used to improve its strength, ductility, and fatigue resistance. As additively manufactured component go through repeated cycles of rapid heating and rapid cooling, significant fraction of undesirable metastable phases are formed. Thus, heat treatment is a crucial step for AM component for dissolution of undesirable phases and precipitation of strengthening phase.

However, it has been found that heat treatment can also affect the residual stresses in the printed component. Residual stresses can be introduced during the additive manufacturing process due to high thermal gradients, solidification, and other factors[27]. These stresses can affect the mechanical properties and performance of the material, and so it is important to understand how heat treatment affects them. The microscopy analysis of the SLM IN718 parts revealed that the printing parameters and heat treatment conditions significantly affected the porosity and microstructure. The optical microstructure results showed in Fig. 5 have a significant change in porosity variation with respect to process parameters. HIP + STA was able to reduce pores to size when compared to STA.

Using the previous literature on densification [1, 2] the sample with LP – 300 W and SS – 1400 mm/s, having lowest density and the changes observed in microstructure with various heat treatment (see Fig. 5). Figure 5 presents polished optical microstructures of IN718 samples produced under three different SLM parameter sets. Sno. 3 (LP = 300 W, SS = 1400 mm/s; density = 8.101 g/cc), S. No. 5 (LP = 360 W, SS = 960 mm/s; density = 8.198 g/cc), and S. No. 7 (LP = 400 W, SS = 520 mm/s; density = 7.949 g/cc)across the AP, STA, and HIP + STA heat-treatment conditions. At Sno. 3, numerous irregular pores are visible in the AP condition, with only slight reduction after STA and partial elimination after HIP + STA. The optimal VED condition (Sno. 5) shows minimal porosity in the AP sample, which further reduces to nearly pore-free condition after HIP + STA, corresponding to the highest measured density. Whereas in Sno. 7 exhibits large spherical keyhole pores in the AP state, which remain prominent after STA and are only partially reduced after HIP + STA. Figure 5 confirms that porosity is strongly

governed by density, with low and high density producing lack-of-fusion and keyhole defects, respectively, while HIP is most effective when the initial porosity is low, as seen in the optimal VED condition.

These mechanical trends directly reflect the underlying microstructural transformations induced by the different heat treatment routes.

Figure 6 compares the microstructural evolution of additively manufactured samples processed under three different volumetric energy density (VED), process parameters and post-processing conditions: as-printed (AP), solution treated and aged (STA), and hot isostatic pressing followed by STA (HIP + STA). The selected samples correspond to Test No. 3 (lowest VED = 48 J/mm³), Test No. 5 (optimal VED = 85 J/mm³), and Test No. 7 (maximum VED = 174 J/mm³), representing low, optimal, and high energy input regimes, respectively.

In the AP condition, all samples exhibit characteristic features of laser powder bed fusion, including visible porosity, and a fish-scale melt pool morphology. These melt pool boundaries arise from rapid solidification and cyclic thermal gradients inherent to the process and are most prominent at lower VED (Test No. 3), where insufficient energy input leads to lack-of-fusion type defects and pronounced microstructural heterogeneity. With increasing VED (Tests No. 5 and 7), melt pools become wider and more continuous, though porosity and anisotropic grain structures are still evident.

After solution treatment and aging (STA), the microstructure shows a significant reduction or near elimination of melt pool boundaries, indicating enhanced diffusion and microstructural homogenization during heat treatment. However, long and thin columnar grains aligned along the build direction persist, and residual porosity can still be observed, particularly in samples fabricated at suboptimal or excessively high VEDs. This behavior is consistent with reported literature, where STA alone is insufficient to fully close process-induced pores or to completely break down the solidification-driven columnar grain structure.

Following HIP + STA, a pronounced transformation in microstructure is observed across all VED conditions. Porosity is effectively eliminated due to the combined action of high temperature and isostatic pressure during HIP. Moreover, the previously observed columnar grains are replaced by a homogeneous, recrystallized equiaxed grain structure, indicating complete recrystallization and grain boundary reconfiguration. This microstructural state reflects the most uniform and defect-free condition, highlighting the effectiveness of HIP combined with STA in mitigating additive manufacturing-induced defects and anisotropy.

3.2 Effect of Heat Treatment on Hardness

The evolution of microstructure and its correlation with mechanical response were studied for the optimal parameter condition (LP = 360 W, SS = 960 mm/s) can be seen in Fig. 7. In the as-printed (AP) state, the alloy exhibited fine columnar grains with distinct melt pool boundaries and residual porosity, resulting in moderate hardness (~ 360 HV) and correspondingly lower strength. Following solution treatment and aging (STA), the elimination of melt pool boundaries and precipitation of strengthening γ'/γ" phases led to a pronounced increase in hardness (~ 540 HV) and tensile strength. However, after hot isostatic pressing followed by STA (HIP + STA), a slight reduction in strength and hardness (~ 535 HV) was observed, attributable to grain coarsening at elevated HIP temperatures, even though porosity was effectively removed. This (as Printed sample) microstructural transition from fine columnar to equiaxed recrystallized(seen in HIP + STA) grains enhances structural homogeneity and ductility, while the STA condition remains the most influential in improving strength and hardness through precipitation hardening.

4. Conclusions

This work optimized the SLM processing of IN718 using a modified Taguchi approach and evaluated the influence of heat treatments and build orientations on mechanical and microstructural performance. Based on the conducted experiments and detailed analyses, the following conclusions are established:

- A laser power of 360 W and scanning speed of 960 mm/s produced the best balance of strength and ductility, yielding the highest density and minimal porosity.

- In the as-printed condition, IN718 exhibited YS = 774 ± 96 MPa, UTS = 1141 ± 81 MPa, and %El = 31 ± 10%.
- After STA, strength improved significantly (YS = 1286 ± 129 MPa, UTS = 1516 ± 130 MPa) due to γ'/γ" precipitation, although elongation decreased to 22 ± 4%.
- HIP + STA further enhanced densification and reduced defect scatter, resulting in a slight reduction in strength (YS = 1163 ± 171 MPa, UTS = 1444 ± 64 MPa) while maintaining elongation similar to STA (21 ± 3%).
- Build orientation effects revealed that XY builds demonstrated higher strength, whereas XZ builds showed ~ 20–25% higher ductility, confirming the inherent anisotropy of the LPBF process.

Analysis of porosity across different density and VED conditions highlighted the critical role of processing parameters. Low-VED samples exhibited irregular lack-of-fusion pores, high-VED samples contained large spherical keyhole pores, and the optimal-VED condition achieved the highest density (8.198 g/cc) with minimal porosity. HIP + STA resulted in negligible porosity, promoted recrystallized equiaxed grains, and reduced scatter in mechanical properties. Samples produced under optimal parameters showed high density and minimal defects even without HIP, indicating that HIP is unnecessary when energy input is properly tuned.

Overall, the combined use of optimized SLM parameters and suitable post-processing provides a reliable pathway for fabricating dense, defect-free IN718 with mechanical properties comparable to wrought alloys. These findings advance the alloy's applicability in aerospace components requiring high strength, fatigue resistance, and structural reliability. Future work may focus on correlating creep and fatigue performance of these optimized IN718 builds under elevated temperature conditions.

Declarations

Author Contribution

Kurre Prasanth Kumar Reddy: Writing review & editing, writing original draft, and formal analysis. Sheela Singh: Review & editing, supervision, data validation. Kartikey Sharma: Material preparation, data collection, writing – review & editing. Boggarapu Nageswara Rao: Review & editing, data validation, supervision, conceptualization, and formal analysis. SVS Narayana Murty: Review & editing original draft, Supervision, Data validation, Conceptualization. Ravi Ranjan Kumar: Review & editing original draft, Data validation, Supervision.

References

1. Reddy KPK, Rao BN, Nazeemudheen MN, Manwatkar SK, Murty SVSN (2023) Selection of Optimal Process Parameters to Obtain Defect-Free Builds in IN718 Made by Laser Powder Bed Fusion. J Mater Eng Perform 33(19):10228–10241. https://doi.org/10.1007/s11665-023-08677-9
2. Reddy KPK, Rao BN, Sharma K, Kumar RR, Murty SVSN (2025) Mechanical Properties of Laser Powder Bed Fusion Processed IN718: Taguchi Optimisation and Analysis of Experimental Results. Lasers Manuf Mater Process 12(3):465–487. https://doi.org/10.1007/s40516-025-00294-9
3. Zhi Q, Niu J, Tan X, Pei R, Liu Y, Chen Y, Liu W (2023) Effect of Scanning Process and Heat Treatment on Microstructure and Mechanical Property of Inconel 718 Fabricated by Selective Laser Melting. J Mater Eng Perform 32(21):9515–9524. https://doi.org/10.1007/s11665-023-07828-2
4. Lu Yanjin W, Songquan G, Yiliang H, Tingting Y, Chuanguang J, Lin, and Lin Jinxin (2015) Study on the Microstructure, Mechanical Property and Residual Stress of SLM Inconel-718 Alloy Manufactured by Differing Island Scanning Strategy. Opt Laser Technol 75:197–206. https://doi.org/10.1016/J.OPTLASTEC.2015.07.009
5. Pradeep PI, Kumar VA, Venkateswaran T, Aswin S, Nair VS, Krishnan A, Akhil, Agilan M, Singh SK, Narayanan PR (2021) Processing and Characterization of 3D-Printed Inconel-718 Component through Laser Powder Bed Fusion Route for High-Temperature Space Application. Trans Indian Natl Acad Eng 2021 6(1):133–146. https://doi.org/10.1007/S41403-020-00196-6

6. Pandey A, Gaur V (2022) Study on Fatigue Damage in Additively Manufactured IN718 Alloy. Procedia Struct Integr 42:1017–1024. https://doi.org/10.1016/J.PROSTR.2022.12.128
7. Sharma K, Kumar RR, Raj D, Manwatkar S, Joseph SK, K., and, Murty N, S. V. S (2024) Mechanical Properties of Laser Powder Bed Fusion Processed Inconel Alloy IN718 in Different Heat Treatment Conditions through Small Scale Specimen Testing. Theoret Appl Fract Mech 134:104756. https://doi.org/10.1016/J.TAFMEC.2024.104756
8. Wang W, Wang S, Zhang X, Chen F, Xu Y, Tian Y (2021) Process Parameter Optimization for Selective Laser Melting of Inconel 718 Superalloy and the Effects of Subsequent Heat Treatment on the Microstructural Evolution and Mechanical Properties. J Manuf Process 64:530–543. https://doi.org/10.1016/J.JMAPRO.2021.02.004
9. Cai C, Gao X, Teng Q, Li M, Pan K, Song B, Yan C, Wei Q, Shi Y (2018) Mater Sci Engineering: A 717:95–104. https://doi.org/10.1016/J.MSEA.2018.01.079. A Novel Hybrid Selective Laser Melting/Hot Isostatic Pressing of near-Net Shaped Ti-6Al-4V Alloy Using an in-Situ Tooling: Interfacial Microstructure Evolution and Enhanced Mechanical Properties
10. Raghavan S, Zhang B, Wang P, Sun CN, Nai MLS, Li T, Wei J (2017) Effect of Different Heat Treatments on the Microstructure and Mechanical Properties in Selective Laser Melted INCONEL 718 Alloy. Mater Manuf Processes 32(14):1588–1595. https://doi.org/10.1080/10426914.2016.1257805
11. Kuo YL, Nagahari T, Kakehi K (2018) The Effect of Post-Processes on the Microstructure and Creep Properties of Alloy718 Built Up by Selective Laser Melting. Mater 2018 11(6):996. https://doi.org/10.3390/MA11060996
12. Kuo YL, Kakehi K (2017) Influence of Powder Surface Contamination in the Ni-Based Superalloy Alloy718 Fabricated by Selective Laser Melting and Hot Isostatic Pressing. Met 2017 7(9):367. https://doi.org/10.3390/MET7090367
13. Calandri M, Yin S, Aldwell B, Calignano F, Lupoi R, Ugues D (2019) Texture and Microstructural Features at Different Length Scales in Inconel 718 Produced by Selective Laser Melting. Mater 2019 12(8):1293. https://doi.org/10.3390/MA12081293
14. Gaikwad SD, Ajay P, Dabhade VV, Murty SVSN, Manwatkar S, Prakash U (2024) Mechanical Properties and Microstructural Analysis of Ultra-Fine Grained Ni-Based ODS Alloy Processed by Powder Forging. J Alloys Compd 970:172614. https://doi.org/10.1016/J.JALLCOM.2023.172614
15. Kuo YL, Kakehi K (2017) Influence of Powder Surface Contamination in the Ni-Based Superalloy Alloy718 Fabricated by Selective Laser Melting and Hot Isostatic Pressing. Met 2017 7(9):367. https://doi.org/10.3390/MET7090367
16. McLouth TD, Witkin DB, Lohser JR, Sitzman SD, Adams PM, Lingley ZR, Bean GE, Yang JM, Zaldivar RJ (2021) Temperature and Strain-Rate Dependence of the Elevated Temperature Ductility of Inconel 718 Prepared by Selective Laser Melting. Mater Sci Engineering: A 824:141814. https://doi.org/10.1016/J.MSEA.2021.141814
17. du Plessis A, Macdonald E (2020) Hot Isostatic Pressing in Metal Additive Manufacturing: X-Ray Tomography Reveals Details of Pore Closure. Addit Manuf 34:101191. https://doi.org/10.1016/J.ADDMA.2020.101191
18. Rezaei A, Rezaeian A, Kermanpur A, Badrossamay M, Foroozmehr E, Marashi M, Foroozmehr A, Han J (2020) Microstructural and Mechanical Anisotropy of Selective Laser Melted IN718 Superalloy at Room and High Temperatures Using Small Punch Test. Mater Charact 162:110200. https://doi.org/10.1016/J.MATCHAR.2020.110200
19. ASTM (2014) ASTM F3055-14 Standard Specification for Additive Manufacturing Nickel Alloy (UNS N07718) with Powder Bed Fusion, ASTM International (2014). https://doi.org/10.1520/F3055-14AR21
20. Salman OO, Brenne F, Niendorf T, Eckert J, Prashanth KG, He T, Scudino S (2019) Impact of the Scanning Strategy on the Mechanical Behavior of 316L Steel Synthesized by Selective Laser Melting. J Manuf Process 45:255–261. https://doi.org/10.1016/J.JMAPRO.2019.07.010
21. Prasanth Kumar RK, Boggarapu NR, Murty N, S. V. S (2023) Multi-Objective Optimization to Specify Optimal Selective Laser Melting Process Parameters for SS316 L Powder. Multidiscipline Model Mater Struct 20(1):59–80. https://doi.org/10.1108/MMMS-06-2023-0213
22. Syed K, Ali MA, Reddy KPK, Rao BN (2023) Analyzing the Influence of Tool Profile on Friction Stir Process with Taguchi Optimization and Tungsten Nano Powder. Int J Veh Struct Syst 15(6):802–807. https://doi.org/10.4273/ijvss.15.6.12
23. Kumar P, Kurre R, Rao Boggarapu N, Sharma K, Kumar RR, Murty N (2025) Optimization of Selective Laser Melting Parameters and Post-Processing for Enhanced Mechanical Properties of IN718 Superalloy. Rapid Prototyp J 1–17. https://doi.org/10.1108/RPJ-07-2025-0292

24. Rajyalakshmi. K, Nageswara Rao B (2019) Expected Range of the Output Response for the Optimum Input Parameters Utilizing the Modified Taguchi Approach. Multidiscipline Model Mater Struct 15(2):508–522. https://doi.org/10.1108/MMMS-05-2018-0088
25. Kumar Reddy KP, Kumar SR, Nageswara Rao B (2024) Multi-Objective Optimization for Minimize Cutting Force and Power Consumption in Corn Stalk Chopping Processes. Heliyon 10(15). https://doi.org/10.1016/j.heliyon.2024.e35373
26. Sri Manikanta K, Suthapalli L, Kurre PKR, Vemuri SA, Boggarapu NR, Anantha MT (2025) Selection of Hyper-Elastic Materials and Pattern of Differentiated Soft Pads Emulating Human Finger Compliance in Robotic Fingertips. Multidiscipline Model Mater Struct 1–14. https://doi.org/10.1108/MMMS-04-2025-0138
27. Mercelis P, Kruth JP (2006) Residual Stresses in Selective Laser Sintering and Selective Laser Melting. Rapid Prototyp J 12(5):254–265. https://doi.org/10.1108/13552540610707013

Figures

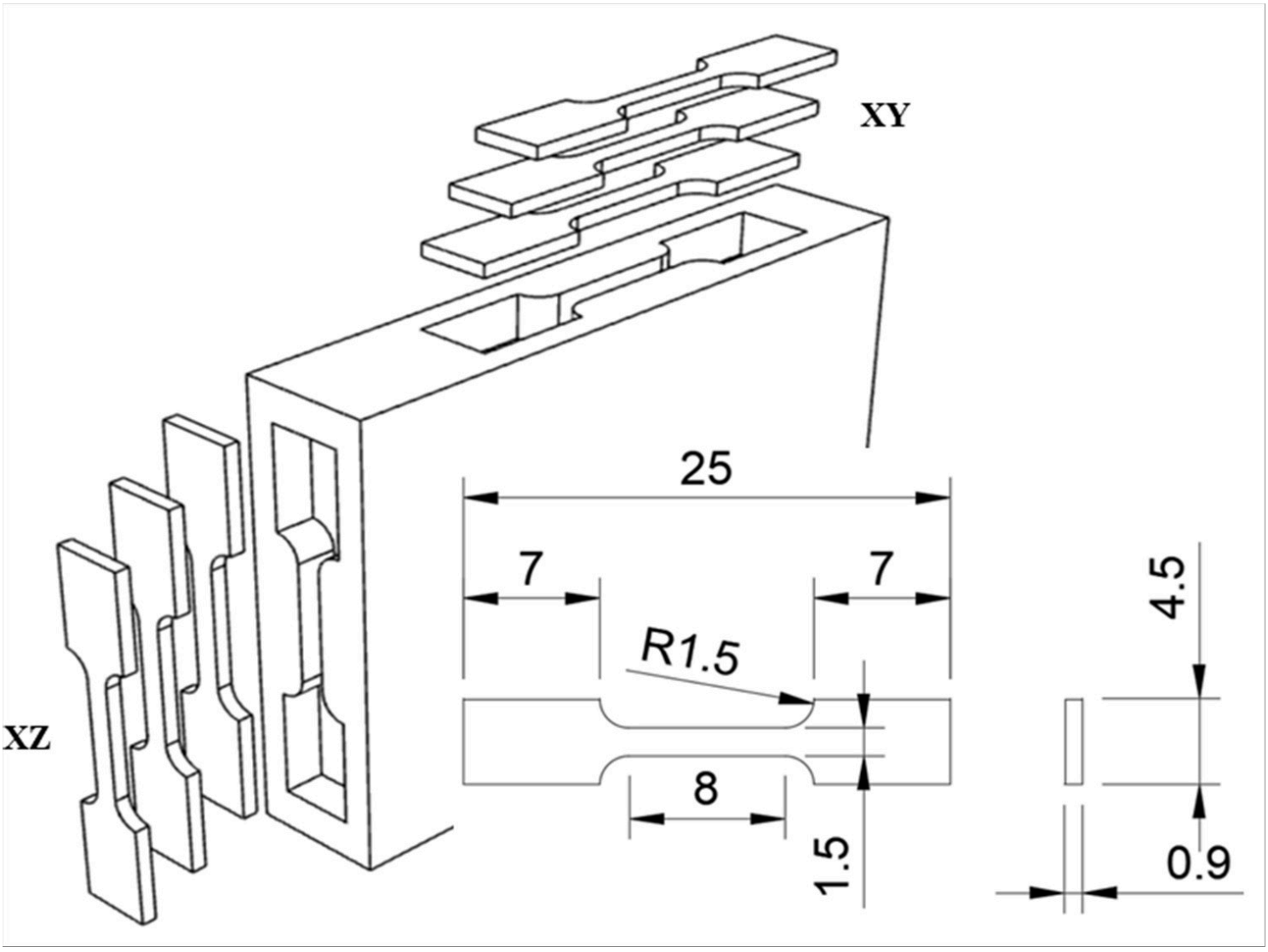

Figure 1

Schematic representation of tensile specimens for both build directions.



Figure 2(a). Comparison of measured %elongation in XY- build direction with the range of estimates for the full factorial design of experiments.

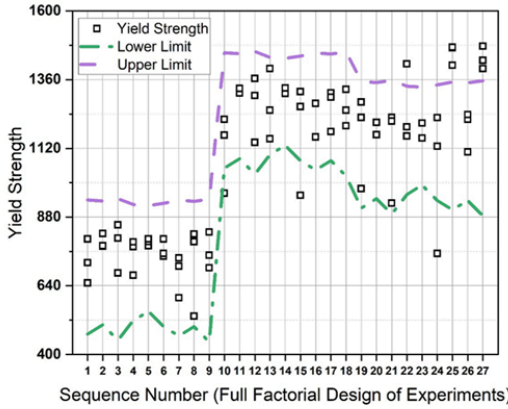

Figure 2(b). Comparison of measured yield strength (YS) in XY- build direction with the range of estimates for the full factorial design of experiments.

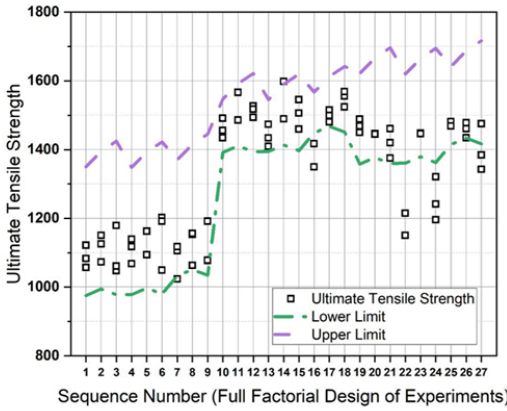

Figure 2(c). Comparison of measured ultimate tensile strength (UTS) in XY- build direction with the range of estimates for the full factorial design of experiments.

Figure 2

See image above for figure legend

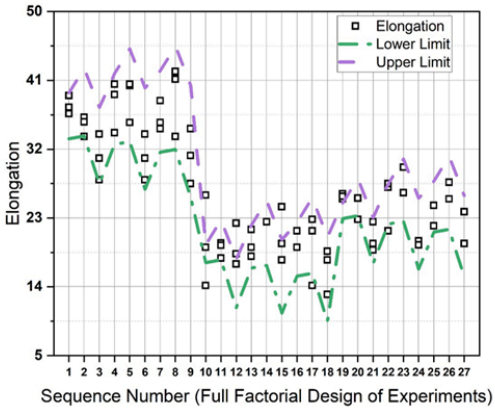

Figure 3(a). Comparison of measured %elongation in XZ- build direction with the range of estimates for the full factorial design of experiments.

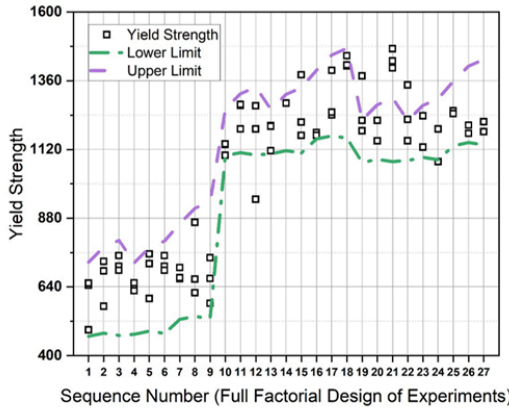

Figure 3(b). Comparison of measured Yield strength (YS) in XZ- build direction with the range of estimates for the full factorial design of experiments.

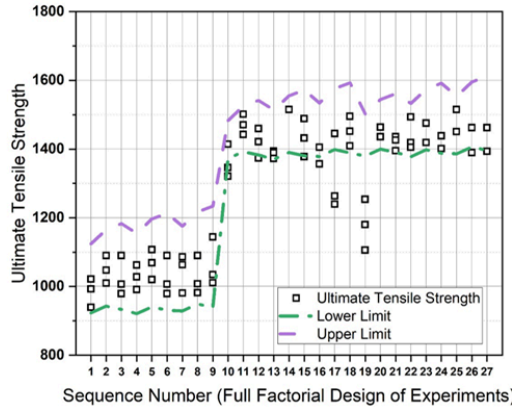

Figure 3(c). Comparison of measured ultimate tensile strength (UTS) in XZ- build direction with the range of estimates for the full factorial design of experiments.

Figure 3

See image above for figure legend

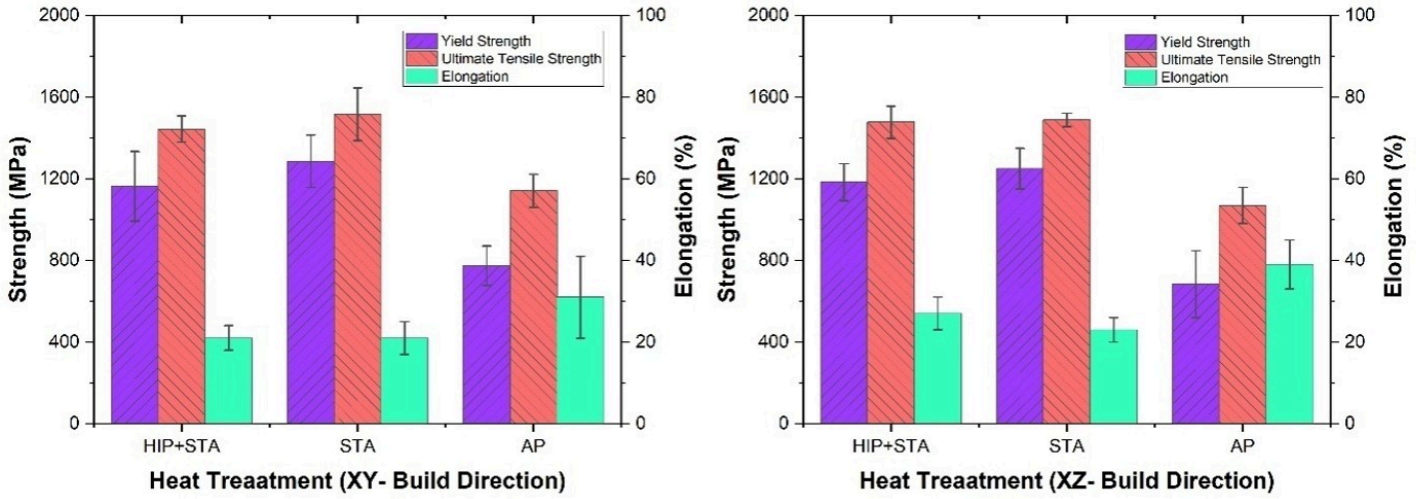

Figure 4

Bar graph of the Strength Values in both XY and XZ build direction

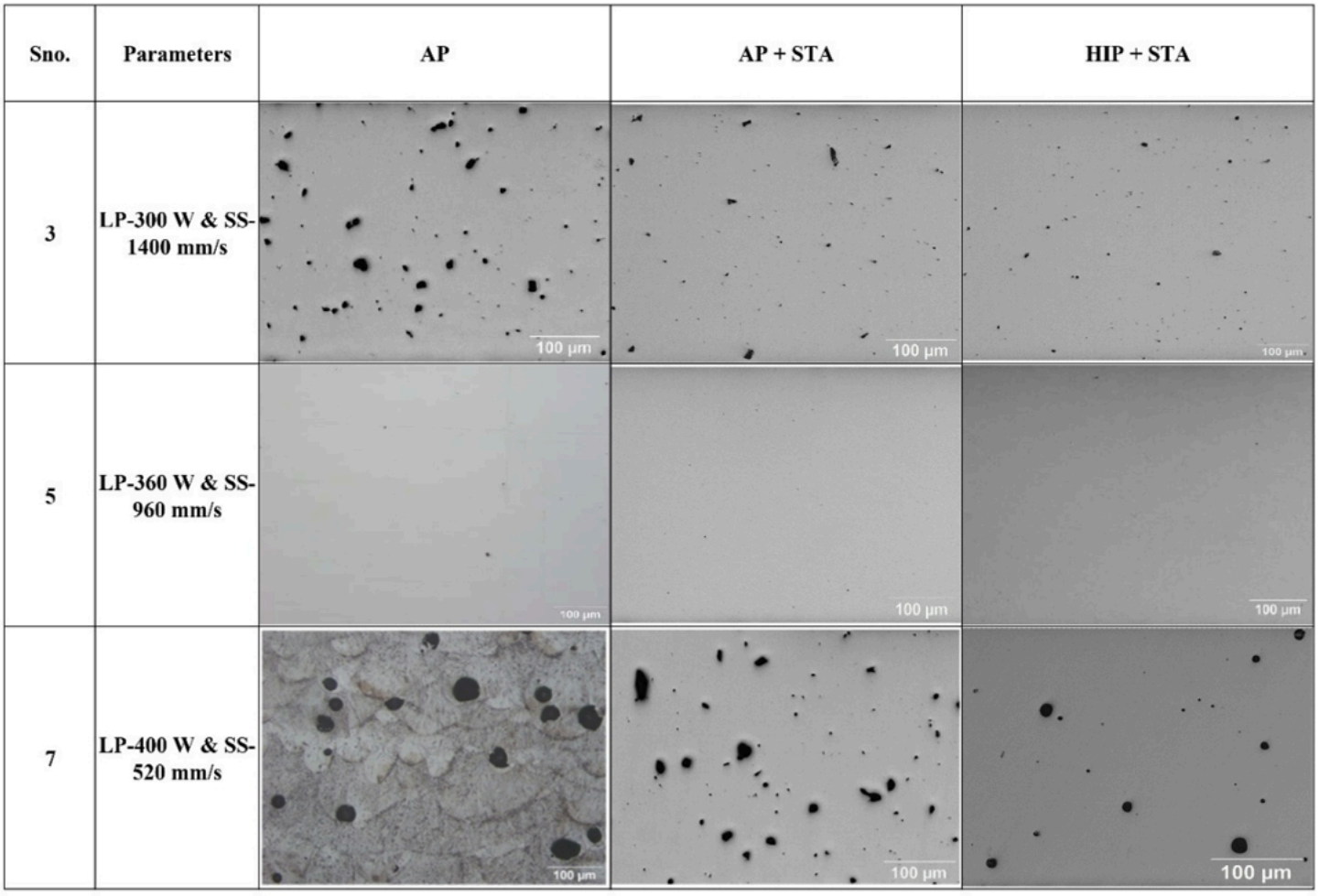

Figure 5

Effect of Various Heat Treatments on the IN718 samples in XY build direction

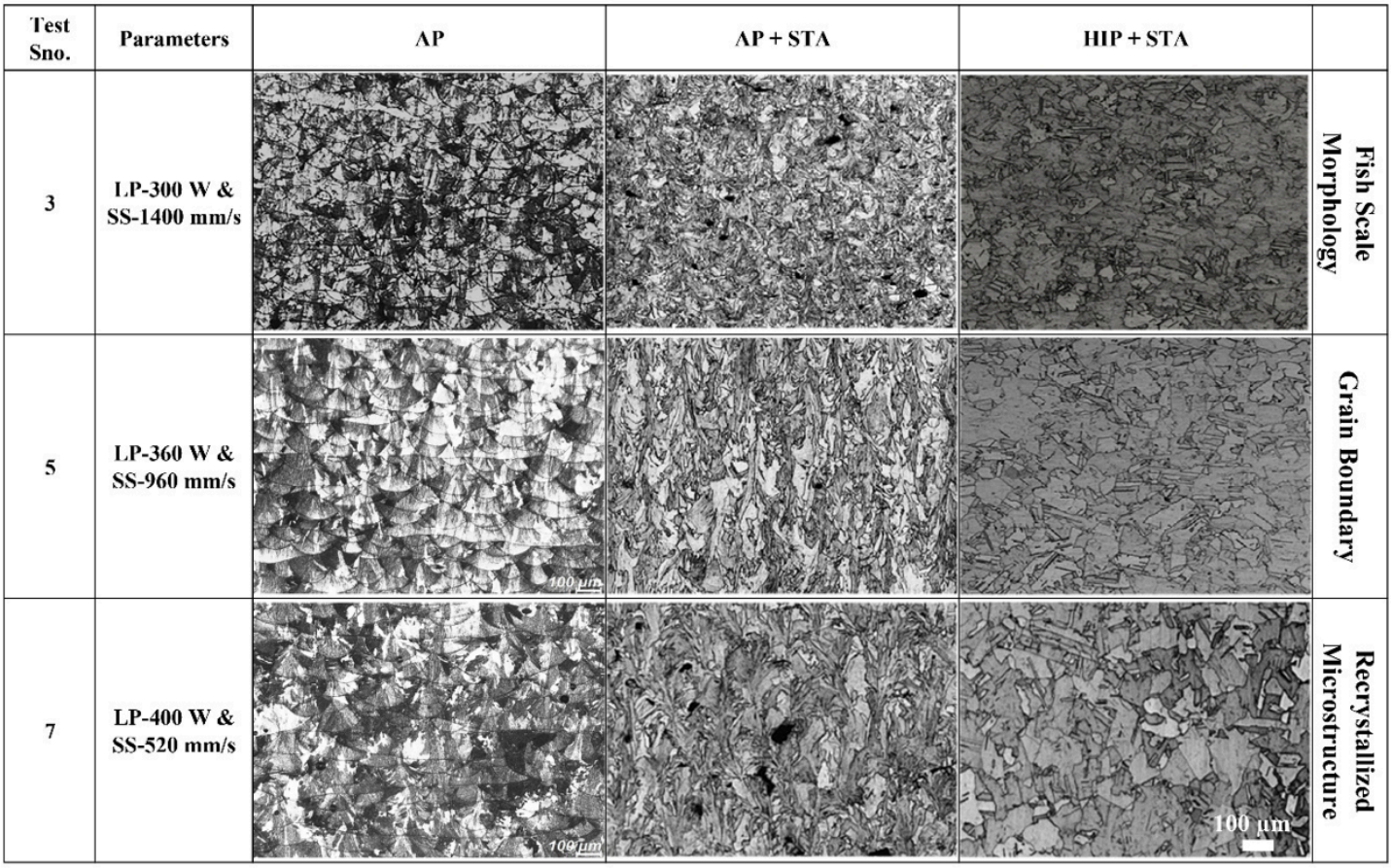

Figure 6

Effect of Various Heat Treatments on the IN718 etched samples in XY build direction

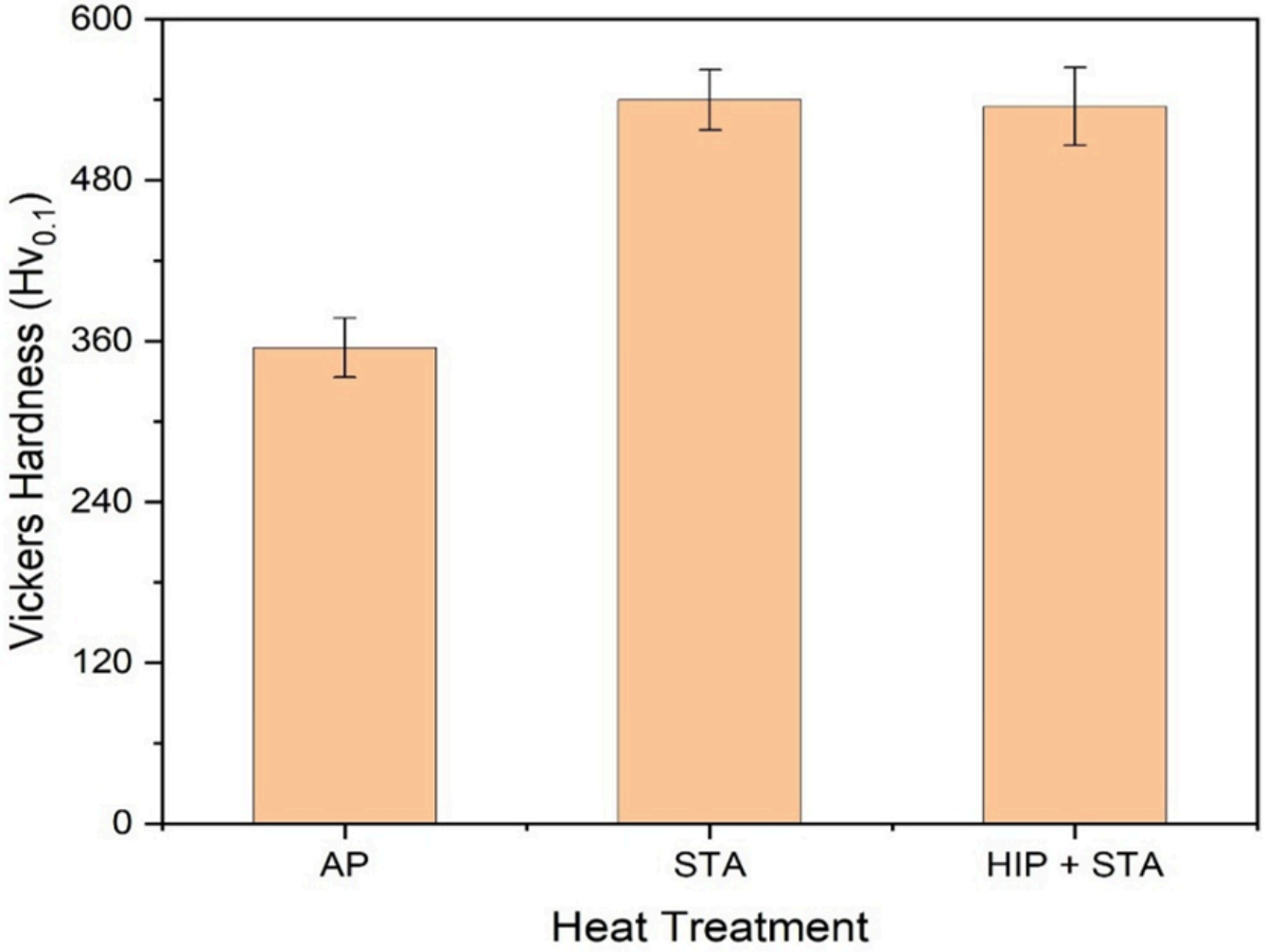

Figure 7

Average Hardness for the different heat treatment